Please cite this article in press as: Luna-Sanchez et al., *Opa1* Overexpression Protects from Early-Onset *Mpv17*$^{-/-}$-Related Mouse Kidney Disease, Molecular Therapy (2020), https://doi.org/10.1016/j.ymthe.2020.06.010

Molecular Therapy
Original Article

Opa1 Overexpression Protects from Early-Onset *Mpv17*$^{-/-}$-Related Mouse Kidney Disease

Marta Luna-Sanchez,[1] Cristiane Benincá,[1] Raffaele Cerutti,[1] Gloria Brea-Calvo,[2] Anna Yeates,[7] Luca Scorrano,[3,4] Massimo Zeviani,[3,5,] and Carlo Viscomi[6,]

[1]University of Cambridge - MRC Mitochondrial Biology Unit, The Keith Peters Building, Cambridge Biomedical Campus, Hills Road, Cambridge CB2 0XY, UK; [2]Centro Andaluz de Biología de Desarrollo and CIBERER, ISCIII, Universidad Pablo de Olavide-CSIC-JA, 41013 Sevilla, Spain; [3]Venetian Institute of Molecular Medicine, Via Orus 2, 35128 Padova, Italy; [4]Department of Biology, University of Padova, via Ugo Bassi 58/B, 35131 Padova, Italy; [5]Department of Neurosciences, University of Padova, via Giustiniani 2, 35128 Padova, Italy; [6]Department of Biomedical Sciences, University of Padova, via Ugo Bassi 58/B, 35131 Padova, Italy; [7]Medical Research Council - Laboratory of Molecular Biology, Francis Crick Avenue, Cambridge Biomedical Campus, Cambridge CB2 0QH, UK

Moderate overexpression of *Opa1*, the master regulator of mitochondrial cristae morphology, significantly improved mitochondrial damage induced by drugs, surgical denervation, or oxidative phosphorylation (OXPHOS) defects due to specific impairment of a single mitochondrial respiratory chain complex. Here, we investigated the effectiveness of this approach in the *Mpv17*$^{-/-}$ mouse, characterized by profound, multisystem mitochondrial DNA (mtDNA) depletion. After the crossing with *Opa1*^{tg} mice, we found a surprising anticipation of the severe, progressive focal segmental glomerulosclerosis, previously described in *Mpv17*$^{-/-}$ animals as a late-onset clinical feature (after 12–18 months of life). In contrast, *Mpv17*$^{-/-}$ animals from this new "mixed" strain died at 8–9 weeks after birth because of severe kidney failure However, *Mpv17*$^{-/-}$*::Opa1*^{tg} mice lived much longer than *Mpv17*$^{-/-}$ littermates and developed the kidney dysfunction much later. mtDNA content and OXPHOS activities were significantly higher in *Mpv17*$^{-/-}$*::Opa1*^{tg} than in *Mpv17*$^{-/-}$ kidneys and similar to those for wild-type (WT) littermates. Mitochondrial network and cristae ultrastructure were largely preserved in *Mpv17*$^{-/-}$*::Opa1*^{tg} versus *Mpv17*$^{-/-}$ kidney and isolated podocytes. Mechanistically, the protective effect of *Opa1* overexpression in this model was mediated by a block in apoptosis due to the stabilization of the mitochondrial cristae. These results demonstrate that strategies aiming at increasing *Opa1* expression or activity can be effective against mtDNA depletion syndromes.

INTRODUCTION

There is an unmet need for new therapies for mitochondrial diseases. Given the extreme genetic, biochemical, and clinical heterogeneity of mitochondrial disorders, an ideal therapeutic approach should be applicable to more than one single clinical entity. Strategies with potential general applicability to several, if not all, mitochondrial diseases have been proposed over the past 10 years by us and others.[1] These include approaches aimed at (1) increasing mitochondrial biogenesis; (2) clearing dysfunctional organelles by stimulating mitophagy; and, although more controversial, (3) by-passing the mitochondrial respiratory chain (MRC) complex defects by using alternative oxidases or (4) reversing the mitochondrial unfolded stress response. An additional promising approach is based on the moderate overexpression of *Opa1*, which encodes a master regulator of shape and function of mitochondrial cristae. We previously showed that this approach improved the clinical phenotype of the *Ndufs4*$^{-/-}$ mouse, which lacks a small subunit of the P module of the MRC complex I (cI), as well as of the muscle-restricted *Cox15*$^{sm/sm}$, which lacks an enzyme essential for the biosynthesis of COX-specific heme A.[2] We proposed that the stabilization of the defective MRC and supercomplexes (SCs), due to tighter and tidier cristae morphology, mediated the therapeutic effect. In addition, the same approach protected mice from a number of insults leading to altered cristae morphology and decreased oxidative phosphorylation (OXPHOS) proficiency, including denervation, lipopolysaccharide (LPS)-induced liver damage, and ischemia reperfusion in heart and brain.[3] However, the applicability of the *Opa1* overexpression therapy to other genetically determined mitochondrial diseases, such as those due to instability of mitochondrial DNA (mtDNA), has not been investigated. Here, we sought to determine whether *Opa1* overexpression could improve the molecular phenotype of the *Mpv17* knockout (KO) mouse associated with mtDNA depletion, which mimics the molecular features of a severe mitochondrial syndrome in humans due to *MPV17* mutations. *MPV17* encodes a small and highly hydrophobic protein embedded in the inner mitochondrial membrane (IMM), whose function is still unknown. In humans, mutations in *MPV17* cause hepatocerebral mtDNA depletion syndrome (OMIM:

Received 23 March 2020; accepted 8 June 2020;
https://doi.org/10.1016/j.ymthe.2020.06.010.

Correspondence: Carlo Viscomi, PhD, Department of Biomedical Sciences, University of Padova, via Ugo Bassi 58/B, Padova, Italy.
E-mail: carlo.viscomi@unipd.it
Correspondence: Massimo Zeviani, MD, PhD, Department of Neurosciences, University of Padova, via Giustiniani, 2, 35128 Padova, Italy.
E-mail: massimo.zeviani@unipd.it

Please cite this article in press as: Luna-Sanchez et al., *Opa1* Overexpression Protects from Early-Onset *Mpv17*$^{-/-}$-Related Mouse Kidney Disease, Molecular Therapy (2020), https://doi.org/10.1016/j.ymthe.2020.06.010

266810256810),[4] including Navajo neurohepatopathy.[5] This syndrome is characterized by early-onset and profound mtDNA depletion in liver, later complicated by neurological failure and, in some cases, peripheral analgesia with corneal scarring. Milder reduction of mtDNA content in skeletal muscle and, occasionally, multiple mtDNA deletions, in addition to mtDNA depletion in liver, have also been reported.[6,7] The patients surviving the acute hepatic failure, dominated by hypoglycemic crises and cirrhotic evolution of the liver parenchyma, develop a progressive ataxia and neurological impairment. The spectrum of disorders due to mutations in *MPV17* has progressively expanded to include (1) juvenile- and adult-onset axonal sensorimotor polyneuropathy without hepatocerebral involvement;[8,9] (2) neuropathy and leukoencephalopathy with multiple mtDNA deletions in skeletal muscle;[10] and (3) adult-onset neurohepatopathy-plus syndrome with multiple deletions of mtDNA in muscle.[11] The common feature of all these clinical syndromes is mtDNA instability, pointing to a role of MPV17 in mtDNA maintenance. However, the function of the *Mpv17* gene product remains unclear, although several hypotheses have been proposed. For instance, MPV17 has been shown to form a non-selective cation channel, affecting mitochondrial membrane potential and reactive oxygen species (ROS) production.[12,13] Other data suggested that the lack of MPV17 leads to a substantial decrease in deoxyguanosine triphosphate (dGTP) and deoxythymidine triphosphate (dTTP) in mouse liver mitochondria, thus facilitating the incorporation of riboGTP (rGTP), which, in turn, distorts mtDNA and may lead to block of its replication.[14] Accordingly, high levels of rGTP were detected in mtDNA from *Mpv17*$^{-/-}$ livers.[15] Other data showed that reduced *MPV17* expression was associated with impaired deoxythymidine monophosphate (dTMP) synthesis without affecting *de novo* or salvage synthesis of dTMP, suggesting that MPV17 may be involved in maintaining dTMP levels in mitochondria through a still-uncharacterized pathway that may be involved in transporting dTMP or one of its precursors from the cytosol to mitochondria.[16] In zebrafish, *Mpv17* has been related to pyrimidine nucleotide metabolism via impairment of dihydroorotate dehydrogenase.[17] All these observations have been reported in single publications and do need further confirmation. Finally, data on *Saccharomyces cerevisiae* support a role for *Sym1*, the yeast ortholog of *Mpv17*, in the homeostatic control of tricarboxylic acid cycle (TCA) cycle intermediates.[18]

Like mutant *MPV17* patients, *Mpv17*$^{-/-}$ mice are characterized by profound depletion of mtDNA in liver and moderate to mild depletion in other organs, such as skeletal muscle, brain, and kidney. However, despite the profound liver mtDNA depletion and contrary to the severe liver failure that characterizes the patients, *Mpv17*$^{-/-}$ mice survive normally up to 1 year of age except for an invariant graying of their fur occurring around the sixth month of life. However, after the first year of life, they develop a focal segmental glomerulosclerosis, leading to death by 1.5–2.0 years of age.[19] A yet-unexplained finding concerning the *Mpv17*$^{-/-}$ mouse model is the shift of the kidney failure, which led to early death a few weeks after birth in the original strain,[20,21] to a much later and slowly progressive condition that was observed and documented in mouse *Mpv17*$^{-/-}$ mice after several generations.[19]

RESULTS

Early-Onset Kidney Disease in *Mpv17*$^{-/-}$ Mice

In order to generate *Mpv17*$^{-/-}$*::Opa1*^{tg} double recombinant mice, we mated *Mpv17*$^{+/-}$[19,22] and *Opa1*^{tg} mouse strains (Figure S1). The latter expresses *Opa1* to levels slightly higher than those in the controls (CTRs) by targeted insertion of an extra copy of *Opa1* into the *Hprt* locus on the X chromosome.[2,3,23] Surprisingly, we noticed that the first *Mpv17*$^{-/-}$ animals (without *Opa1* extra copies) started to die around 8–9 weeks of age (Figure 1A). This was reminiscent of the original phenotype described for this strain, i.e., an early death due to focal segmental glomerulosclerosis. We termed this strain the "new" *Mpv17*$^{-/-}$ strain, compared to our later onset, slowly progressive "old" *Mpv17*$^{-/-}$ strain. To search for possible modifier genes responsible for the phenotype anticipation, we first analyzed two genes previously proposed to modify the severity of the clinical phenotype in some mouse models of mitochondrial dysfunction, i.e., *Prkdc*, encoding for the catalytic subunit of the DNA-dependent protein kinase (DNA-PK),[24] and *Nnt*, encoding the nicotinamide nucleotide transhydrogenase.[25] However, the *Prkdc* mutation described in BALB/c and other inbred strains was not present in our C57BL/6 colonies, and the *Nnt* mutation, present in the pure C57BL/6J strain, did not segregate with the disease (data not shown). In order to identify potential genetic modifiers, we also carried out a RNA-sequencing (RNA-seq) experiment by analyzing the total RNA extracted from the kidneys of four *Mpv17*$^{-/-}$ mice, obtained after the crossing with the *Opa1*^{tg} mice, and showing early-onset kidney failure compared with the RNA of four animals belonging to our original, long-surviving, *Mpv17*$^{-/-}$ strain, sacrificed at 1 month of age, i.e., in a pre-symptomatic stage in both strains. The results are summarized in the volcano plot in Figure S2A. We found that 23 genes were significantly varied in the new strain versus the original strain. Among these, the only mitochondrial ones were *Slc25a48*, encoding an uncharacterized carrier that was upregulated in the new strain, and *Upp2*, encoding the uridine phosphorylase 2 that was downregulated in the new strain. Other gene products differentially expressed in the two strains did not localize in mitochondria, and the most differently expressed target was a non-coding RNA, termed AC158975.2, which was downregulated in the new KO strain. These results are also reported in detail in Figure S2B.

Opa1 Moderate Overexpression Prolongs the Lifespan of *Mpv17*$^{-/-}$ Mice by Preventing Early-Onset Glomerulosclerosis

To investigate the presence of kidney failure in our strains, we measured proteinuria by using semiquantitative strips. All tested "new" *Mpv17*$^{-/-}$ animals displayed high proteinuria compared to the CTR littermates (n = 8 per group) (Figure S3A). Necroscopic analysis of 8-week-old mice revealed that the kidneys were smaller and weighted less in *Mpv17*$^{-/-}$ versus CTR littermates (Figures S3B and S3C), which included both *Mpv17*$^{+/+}$ and *Mpv17*$^{+/-}$ individuals. Hematoxylin and eosin (H&E) staining showed the presence of many degenerating glomeruli and some protein casts in the tubuli of *Mpv17*$^{-/-}$ (Figure 1B) but neither in the tubuli of CTR nor of

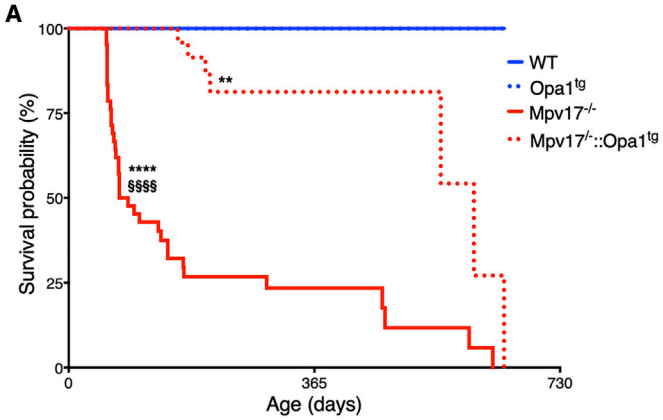

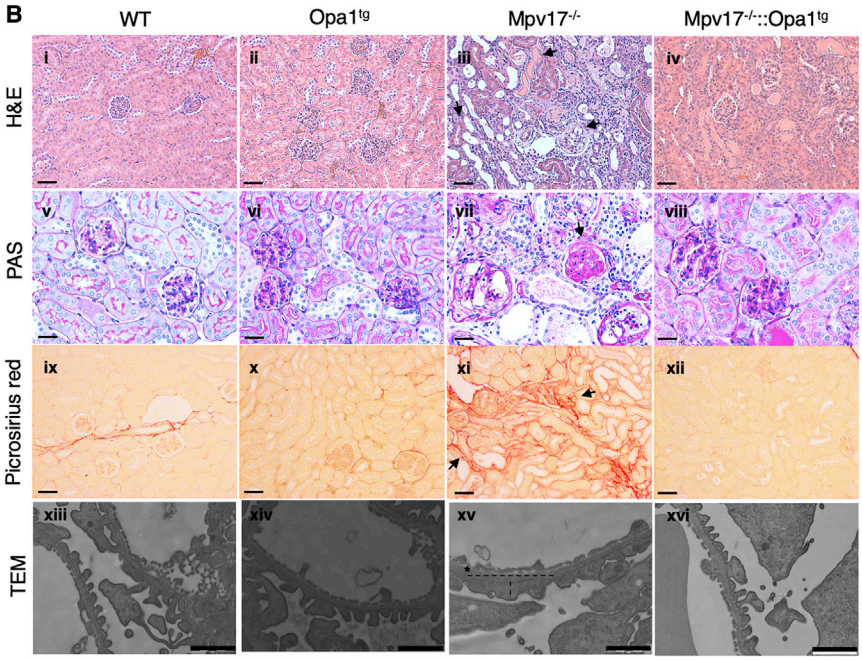

Figure 1. Effects of Opa1 Overexpression on Survival Probability and Kidney Disease of *Mpv17*$^{-/-}$ Mice

(A) Kaplan-Meier analysis of WT, *Opa1*^{tg}, *Mpv17*$^{-/-}$, and *Mpv17*$^{-/-}$::*Opa1*^{tg} mice (n = 30). Kaplan-Meier survival probability. Significance was assessed by the log-rank test. Symbols * and § represent the significance levels of *Mpv17*$^{-/-}$::*Opa1*^{tg} versus WT and *Mpv17*$^{-/-}$, respectively: ****p < 0.0001 (*Mpv17*$^{-/-}$ vs. WT); **p = 0.0067 (*Mpv17*$^{-/-}$::*Opa1*^{tg} vs. WT); §§§§p < 0.0001 (*Mpv17*$^{-/-}$::*Opa1*^{tg} vs. *Mpv17*$^{-/-}$). (B) Histological characterization of WT, *Opa1*^{tg}, *Mpv17*$^{-/-}$, and *Mpv17*$^{-/-}$::*Opa1*^{tg} kidneys. Scale bars: 50 μm for all the light microscopy staining except for PAS, for which the scale bars represent 20 μm. TEM indicates foot process in kidney of the indicated genotypes; dashed lines indicate height and width of foot process, and the asterisk indicates the glomerular basement membrane (GBM). Scale bars: 1 μm.

Opa1^{tg} mice (Figure 1B). Periodic acid-Schiff (PAS) staining revealed the presence of collagen-related glycoproteins in the glomeruli, with partial obliteration of the capillary loops (Figure 1B). Picrosirius-red staining confirmed the massive presence of fibrotic tissue (Figure 1B). Finally, transmission electron microscopy (TEM) showed profoundly altered podocytes in the glomeruli with loss of the foot processes (Figures 1B and S3D). These data confirmed the presence of an early-onset and severe focal segmental glomerulosclerosis in the "new" *Mpv17*$^{-/-}$ mouse strain. However, *Opa1* overexpression had a striking protective effect so that *Mpv17*$^{-/-}$:: *Opa1*^{tg} mice lived significantly longer than naive *Mpv17*$^{-/-}$ littermates (median lifespan: 553 vs. 75 days) (Figure 1A) and showed only minor histological alterations (Figure 1B).

Opa1 Overexpression Prevents OXPHOS Defects by Increasing mtDNA Content in Kidney

Profound mtDNA depletion in liver and more moderate in kidney is a hallmark of *Mpv17*$^{-/-}$ mice.[19] We thus investigated whether *Opa1* overexpression was able to increase mtDNA content in these tissues. We found that liver mtDNA content was doubled in *Mpv17*$^{-/-}$::*Opa1*^{tg} mice compared to "new" *Mpv17*$^{-/-}$ animals (10.92 ± 2.33 vs. 4.31 ± 2.28; p < 0.01; n = 6 per genotype), but it was still markedly lower than in wild-type (WT) or *Opa1*^{tg} littermates (100 ± 33 and 106 ± 20, respectively; p < 0.0001; n = 6) (Figure S4A). Accordingly, the spectrophotometric activities of MRC complexes cI, $cIII_2$, and cIV in liver homogenates were no different between *Mpv17*$^{-/-}$::*Opa1*^{tg} and *Mpv17*$^{-/-}$, and both were significantly lower than in the CTR and *Opa1*^{tg} groups (Figure S4B), despite *Opa1* overexpression being confirmed in the liver of *Mpv17*$^{-/-}$:: *Opa1*^{tg} versus *Mpv17*$^{-/-}$ animals (Figure S4C).

We then analyzed the kidneys, the most affected organ in this "new" *Mpv17*$^{-/-}$ model characterized by early-onset disease. First, we confirmed that *Opa1* was overexpressed in *Opa1*^{tg} and *Mpv17*$^{-/-}$::*Opa1*^{tg} compared to WT and *Mpv17*$^{-/-}$ by real-time PCR (Figure S5A) and western blot immunovisualization (Figures S5B and S5C). Notably, the amount of OPA1 was reduced in *Mpv17*$^{-/-}$ kidneys but was similar to that of *Opa1*^{tg} in *Mpv17*$^{-/-}$::*Opa1*^{tg}. Second, we measured mtDNA content. Similarly to that in liver, mtDNA content was doubled in *Mpv17*$^{-/-}$:: *Opa1*^{tg} versus *Mpv17*$^{-/-}$ kidneys (69 ± 13.5 vs. 33 ± 21.1). The mtDNA

Please cite this article in press as: Luna-Sanchez et al., *Opa1* Overexpression Protects from Early-Onset *Mpv17*$^{-/-}$-Related Mouse Kidney Disease, Molecular Therapy (2020), https://doi.org/10.1016/j.ymthe.2020.06.010

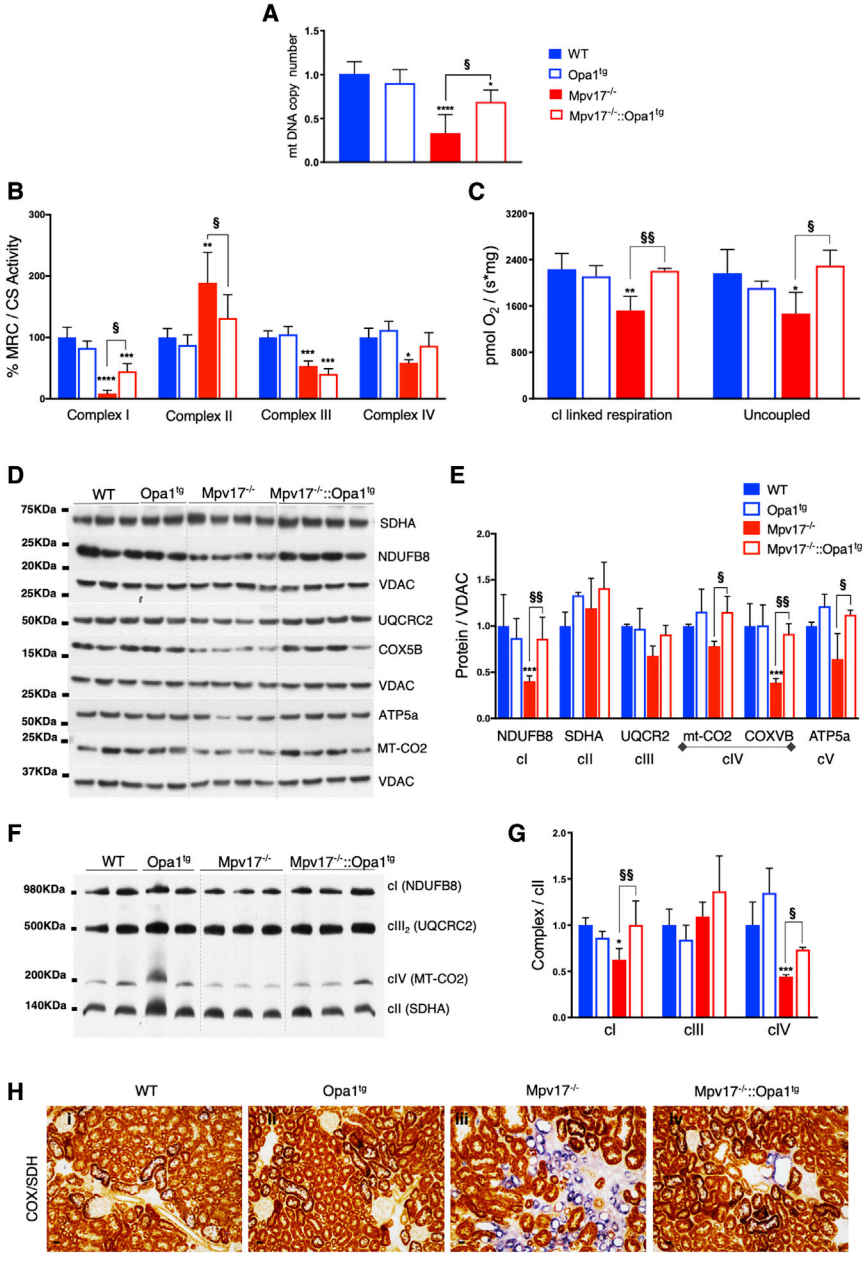

Figure 2. Effects of Opa1 Overexpression on mtDNA Content and Respiratory Chain of *Mpv17*$^{-/-}$

(A) mtDNA copy number in WT, *Opa1*^{tg}, *Mpv17*$^{-/-}$, and *Mpv17*$^{-/-}$*::Opa1*^{tg} kidneys (5 mice per genotype). Data are shown as mean ± SD. Symbols * and § represent the significance levels of *Mpv17*$^{-/-}$*::Opa1*^{tg} versus WT and *Mpv17*$^{-/-}$, respectively, calculated by one-way ANOVA with Tukey's post hoc multiple comparison test: ****p < 0.0001 (*Mpv17*$^{-/-}$ vs. WT); *p = 0.01 (*Mpv17*$^{-/-}$*::Opa1*^{tg} vs. WT); §p = 0.0137 (*Mpv17*$^{-/-}$*::Opa1*^{tg} vs. *Mpv17*$^{-/-}$). (B) MRC activities normalized to citrate synthase (CS) in kidney homogenates of WT, *Opa1*^{tg}, *Mpv17*$^{-/-}$, and *Mpv17*$^{-/-}$*::Opa1*^{tg} mice (n = 4 mice per genotype). Data are shown as mean ± SD. Symbols * and § represent the significance levels of *Mpv17*$^{-/-}$*::Opa1*^{tg} versus WT and *Mpv17*$^{-/-}$, respectively, calculated by one-way ANOVA with Tukey's post hoc multiple comparison test. For cI: ****p < 0.0001 (*Mpv17*$^{-/-}$ vs. WT); ***p = 0.009 (*Mpv17*$^{-/-}$*::Opa1*^{tg} vs. WT); §p = 0.04515 (*Mpv17*$^{-/-}$*::Opa1*^{tg} vs. *Mpv17*$^{-/-}$). For cII: **p = 0.0095 (*Mpv17*$^{-/-}$ vs. WT); §p = 0.0479 (*Mpv17*$^{-/-}$*::Opa1*^{tg} vs. *Mpv17*$^{-/-}$). For cIII: ***p = 0.0005 (*Mpv17*$^{-/-}$ vs. WT); ***p = 0.0002 (*Mpv17*$^{-/-}$*::Opa1*^{tg} vs. WT). For cIV: *p = 0.0121 (*Mpv17*$^{-/-}$ vs. WT). (C) High-resolution respirometry on isolated kidney mitochondria from WT, *Opa1*^{tg}, *Mpv17*$^{-/-}$, and *Mpv17*$^{-/-}$*::Opa1*^{tg} mice (n = 4 mice per genotype). Data are shown as mean ± SD. Symbols * and § represent the significance levels of *Mpv17*$^{-/-}$*::Opa1*^{tg} versus WT and *Mpv17*$^{-/-}$, respectively, calculated by one-way ANOVA with Tukey's post hoc multiple comparison test. For cI: **p = 0.0032 (*Mpv17*$^{-/-}$ vs. WT); §§p = 0.0071 (*Mpv17*$^{-/-}$*::Opa1*^{tg} vs. *Mpv17*$^{-/-}$). For uncoupled: *p = 0.0402 (*Mpv17*$^{-/-}$ vs. WT); §p = 0.0236 (*Mpv17*$^{-/-}$*::Opa1*^{tg} vs. *Mpv17*$^{-/-}$). (D) Western-blot immunovisualization of MRC complex subunits in kidney homogenates from the indicated genotypes. (E) Densitometric analysis of the western blot immunovisualization shown in (D) (n = 3 WT; n = 3 *Opa1*^{tg}; and n = 4 *Mpv17*$^{-/-}$). Data are shown as mean ± SD. Symbols * and § represent the significance levels of *Mpv17*$^{-/-}$*::Opa1*^{tg} versus WT and *Mpv17*$^{-/-}$, respectively, calculated by one-way ANOVA with Tukey's post hoc multiple comparison test. For cI: ***p = 0.0007 (*Mpv17*$^{-/-}$ vs. WT); §§p = 0.057 (*Mpv17*$^{-/-}$*::Opa1*^{tg} vs. *Mpv17*$^{-/-}$). For cIV: §p = 0.04 (*Mpv17*$^{-/-}$*::Opa1*^{tg} vs. *Mpv17*$^{-/-}$). For COXVB: ***p = 0.0005 (*Mpv17*$^{-/-}$ vs. WT); §§p = 0.003 (*Mpv17*$^{-/-}$*::Opa1*^{tg} vs. *Mpv17*$^{-/-}$). For cV: §p = 0.0146 (*Mpv17*$^{-/-}$*::Opa1*^{tg} vs. *Mpv17*$^{-/-}$). (F) 1D-BNGE analysis of DDM-solubilized kidney mitochondria from the different genotypes. (G) Densitometric analysis of the western blot immunovisualization shown in (F); n = 4 WT, 4 *Opa1*^{tg}, 7 *Mpv17*$^{-/-}$, and 7 *Mpv17*$^{-/-}$*::Opa1*^{tg}. Data are shown as mean ± SD. Symbols * and § represent the significance levels of *Mpv17*$^{-/-}$*::Opa1*^{tg} versus WT and *Mpv17*$^{-/-}$, respectively, calculated by two-way ANOVA with Tukey's post hoc multiple comparison test. For cI: *p = 0.0218 (*Mpv17*$^{-/-}$ vs. WT); §§p = 0.0045 (*Mpv17*$^{-/-}$*::Opa1*^{tg} vs. *Mpv17*$^{-/-}$). For cIV: ***p = 0.0002 (*Mpv17*$^{-/-}$ vs. WT); §p = 0.0432 (*Mpv17*$^{-/-}$*::Opa1*^{tg} vs. *Mpv17*$^{-/-}$). (H) Histochemical staining for COX in kidneys of WT, *Opa1*^{tg}, *Mpv17*$^{-/-}$, and *Mpv17*$^{-/-}$*::Opa1*^{tg} mice. Scale bars: 10 μm.

amount of double recombinant *Mpv17*$^{-/-}$*:: Opa1*^{tg} animals was, indeed, not significantly different from that of WT and *Opa1*^{tg} mice (100.0 ± 13.0 and 90.0 ± 15.3, respectively) (Figure 2A).

We then analyzed the activities of the MRC complexes in kidney homogenates from animals of the different genotypes. cI- and cIV-specific activities normalized to citrate synthase (CS) activity were significantly higher in *Mpv17*$^{-/-}$*::Opa1*^{tg} *versus Mpv17*$^{-/-}$ samples, although they were still significantly lower than in WT and *Opa1*^{tg} animals (Figure 2B). No differences were detected between *Mpv17*$^{-/-}$*::Opa1*^{tg} versus *Mpv17*$^{-/-}$ in cIII$_2$ activity, which was in both strains lower than in CTR animals. Finally, cII, which was

significantly higher in *Mpv17*$^{-/-}$ kidneys, was comparable to CTR and *Opa1*^{tg} animals in *Mpv17*$^{-/-}$::*Opa1*^{tg} mice. In addition, cI-dependent (rotenone-sensitive) and uncoupled oxygen consumptions, which were both reduced in *Mpv17*$^{-/-}$ mice, were normal in *Mpv17*$^{-/-}$::*Opa1*^{tg} kidney mitochondria (Figure 2C).

Given the aforementioned results, we analyzed the protein levels of several MRC subunits. In agreement with the spectrophotometric activities, cI subunit NDUFB8, cIV subunits mt-CO2 and COX5B, and cV subunit ATP5A were increased in *Mpv17*$^{-/-}$::*Opa1*^{tg} versus *Mpv17*$^{-/-}$ mice (Figures 2D and 2E). No significant changes were detected in cII subunit SDHA and $cIII_2$ subunit UQCR2. Finally, we analyzed respiratory holocomplexes in dodecyl-maltoside (DDM)-solubilized kidney mitochondria by first-dimension blue native gel electrophoresis (1D-BNGE). The amounts of both cI and cIV, which were decreased in *Mpv17*$^{-/-}$ mice, became comparable to those of CTRs in *Mpv17*$^{-/-}$::*Opa1*^{tg} (Figures 2F and 2G). However, western blot analyses of 1D-BNGE in digitonin-treated isolated kidney mitochondria did not show any significant changes in the amount of cI- and $cIII_2$-containing SCs, suggesting that the amelioration of the phenotype in the *Mpv17*$^{-/-}$::*Opa1*^{tg} mice was not related to an increase in the stability of MRC SCs (Figures S5D and S5E). These data were further confirmed by in-gel activity for cI and cI-containing SCs (Figure S5F). Histochemical analysis of kidney sections revealed a decrease in the intensity of COX-specific staining in virtually all glomeruli and uneven distribution of COX staining in the tubuli (Figure 2H) of *Mpv17*$^{-/-}$, as previously reported.[19]

Decreased mtDNA content and expression were previously reported to correlate to mitochondrial coenzyme Q (CoQ) levels.[26] However, we did not find any difference in CoQ levels in homogenates from *Mpv17*$^{-/-}$ and CTR kidneys (Figure S5G).

We then used laser-captured microdissected glomeruli and tubuli from animals of the different genotypes. We analyzed both COX-positive and COX-negative tubuli from *Mpv17*$^{-/-}$ and *Mpv17*$^{-/-}$::*Opa1*^{tg} animals. By quantitative PCR, we found that mtDNA content was particularly low in *Mpv17*$^{-/-}$ glomeruli and COX-negative tubuli (18% and 29% of the CTRs, respectively) (Figures S6A and S6B, respectively). In contrast, no differences were detected in COX-positive tubuli compared to CTRs (Figure S5C). Notably, the mtDNA content in both glomeruli and tubuli was markedly increased in *Mpv17*$^{-/-}$::*Opa1*^{tg} versus *Mpv17*$^{-/-}$ mice, although, in both cases, it remained significantly lower than in WT and *Opa1*^{tg} animals (60% and 68% respectively).

These results indicate that *Opa1* overexpression is preventing mtDNA depletion and mitochondria dysfunction in specific regions of *Mpv17*$^{-/-}$ mouse kidney.

Opa1 Overexpression Prevents Mitochondrial Fragmentation and Preserves Cristae Ultrastructure in *Mpv17*$^{-/-}$ Mice

TEM analysis of the kidneys at low magnification showed a significant reduction in the number of cells in the glomeruli of *Mpv17*$^{-/-}$ kidney sections compared to WT, *Opa1*^{tg}, and *Mpv17*$^{-/-}$::*Opa1*^{tg} (Figures 3A and 3B), with accumulation of abnormal mitochondria with altered cristae in glomerular cells (Figures 3C and 3D). In addition, a mixed population of normal and altered mitochondria was present in different areas of the tubuli of *Mpv17*$^{-/-}$ mice (Figure S7).

Given the reduced number of cells in *Mpv17*$^{-/-}$ glomeruli, we carried out additional experiments in isolated primary podocytes. Since no differences were observed between WT and *Opa1*^{tg} mice, we did not produce *Opa1*^{tg} podocytes.

First, we assessed the purity of the culture by immunostaining with an anti-NPHS2 antibody, which recognizes a specific marker for podocytes, and used an anti-cytokeratin antibody to exclude the presence of epithelial cells (Figure S8). We then quantified mitochondria length and found a significant decrease in the average size of *Mpv17*$^{-/-}$ mitochondria compared to WT, while it was normal in *Mpv17*$^{-/-}$::*Opa1*^{tg} podocytes (Figures 4A and 4B). In keeping with these data, we found that the amount of MFN2, a protein of the outer mitochondrial membrane playing a key role in mitochondrial fusion, was markedly decreased in *Mpv17*$^{-/-}$ kidney homogenates but was comparable to WT in *Mpv17*$^{-/-}$::*Opa1*^{tg} kidneys (Figures 4C and 4D). Next, we quantified mitochondrial ultrastructure in isolated podocytes. A significantly reduced number of cristae and increased cristae junction (CJ) width were found in *Mpv17*$^{-/-}$ versus WT cells (Figures 5A–5C). In contrast, both number and CJ width were similar to WT in *Mpv17*$^{-/-}$::*Opa1*^{tg} cells. Similar to what was observed for MFN2, MIC19, a component of the mitochondrial contact site and cristae organizing system (MICOS) complex involved in cristae shaping,[27] was markedly decreased in *Mpv17*$^{-/-}$ kidney mitochondria but was comparable to WT in *Mpv17*$^{-/-}$::*Opa1*^{tg} kidneys (Figures 5D and 5E). In addition, overexposure of the 1D-BNGE membranes revealed accumulation of the free ATP-synthase F1 particle in *Mpv17*$^{-/-}$ cells, which was not observed in *Mpv17*$^{-/-}$::*Opa1*^{tg} (Figure 5F). These results suggest that *Opa1* overexpression preserves mitochondrial ultrastructure in the absence of *Mpv17*, possibly by increasing mitochondria fusion and leading to the stabilization of the MICOS complex and ATP synthase structure.

Opa1 Overexpression Prevents *Mpv17*-Dependent Glomerulosclerosis by Blocking Apoptosis

We then investigated whether the correction of mitochondrial ultrastructure can lead to the rescue of the glomerulosclerosis and lethality of *Mpv17*$^{-/-}$ mice. As mentioned earlier, a significant reduction in the number of cells in the glomeruli was observed at low magnification in TEM analysis of *Mpv17*$^{-/-}$ kidney sections compared to the WT, *Opa1*^{tg}, and *Mpv17*$^{-/-}$::*Opa1*^{tg} (Figures 3A and 3B). This result, which suggests increased cell death, prompted us to investigate whether *Opa1* overexpression blocked apoptosis in *Mpv17*$^{-/-}$ kidneys. Cleaved caspase-3 immunohistochemistry showed many positive cells, especially in the glomeruli of "new" *Mpv17*$^{-/-}$ kidneys. In contrast, only a few positive cells were detected in *Mpv17*$^{-/-}$::*Opa1*^{tg} samples (Figure 6A). These results were further confirmed by quantification of cleaved caspase-3 in isolated podocytes (Figure 6B).

Please cite this article in press as: Luna-Sanchez et al., *Opa1* Overexpression Protects from Early-Onset *Mpv17*$^{-/-}$-Related Mouse Kidney Disease, Molecular Therapy (2020), https://doi.org/10.1016/j.ymthe.2020.06.010

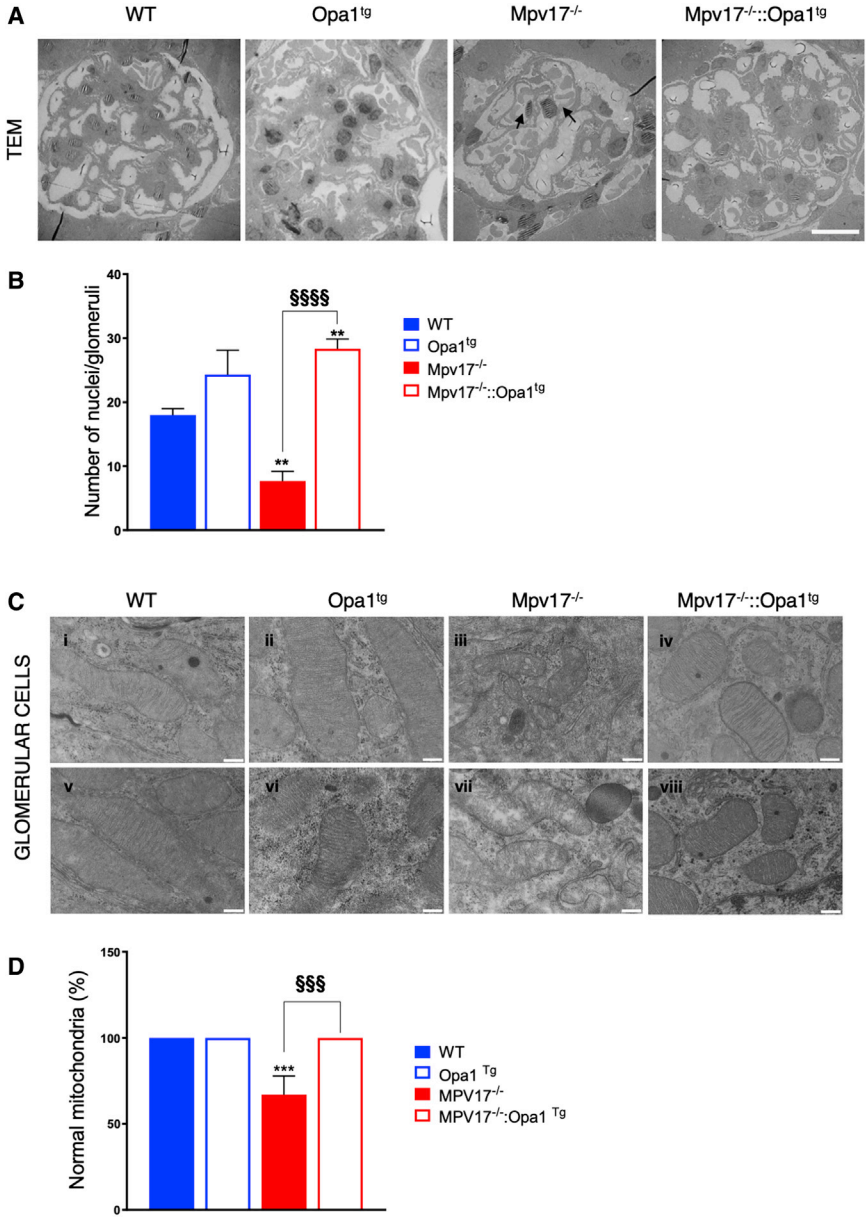

Figure 3. TEM Analysis of *Mpv17*$^{-/-}$ Kidneys

(A) Representative low-magnification TEM micrographs from mouse kidneys of the indicated genotypes showing the glomeruli. Scale bars: 200 nm. (B) Quantification of the number of nuclei per glomerulus in WT, *Mpv17*$^{-/-}$, and *Mpv17*$^{-/-}$*::Opa1*^{tg} kidneys. Data for number of nuclei per glomerulus are plotted as mean ± SD (n = 3). Symbols * and § represent the significance levels of *Mpv17*$^{-/-}$*::Opa1*^{tg} versus WT and *Mpv17*$^{-/-}$, respectively, calculated by one-way ANOVA followed by Tukey's multiple comparison test. **p = 0.0021 (*Mpv17*$^{-/-}$ vs. WT and *Mpv17*$^{-/-}$*::Opa1*^{tg} vs. WT); §§§§p < 0.0001 (*Mpv17*$^{-/-}$*::Opa1*^{tg} vs. *Mpv17*$^{-/-}$). (C) Representative TEM images at high magnification showing the accumulation of damaged mitochondria in *Mpv17*$^{-/-}$ glomeruli. (D) Quantification of the number of damaged mitochondria in glomeruli of the indicated genotypes. Data plotted for number of damaged mitochondria per cell are expressed as mean ± SD (n = 3). Symbols * and § represent the significance levels of *Mpv17*$^{-/-}$*::Opa1*^{tg} versus WT and *Mpv17*$^{-/-}$, respectively, calculated by one-way ANOVA followed by Tukey's multiple comparison test. ***p = 0.0021; *p = 0.0403 (*Mpv17*$^{-/-}$ vs. WT and *Mpv17*$^{-/-}$*::Opa1*^{tg} vs. WT); §§§p = 0.0001; §p = 0.0403 (*Mpv17*$^{-/-}$*::Opa1*^{tg} vs. *Mpv17*$^{-/-}$).

During apoptosis, the proapoptotic factor BAX translocates from cytoplasm to the mitochondrial outer membrane, promoting the release of cytochrome *c*, which, in turn, interacts with APAF1, activating the caspase cascade (Figure 7A). Caspase-3 activation also causes the cleavage of the pro-autophagic factor Beclin-1 in three fragments of 50, 37 and 35 kDa. Cleaved BECLIN-1 cannot activate autophagy, and the 50-kDa N-terminal fragment re-localizes to both nucleus and mitochondria, enhancing the apoptotic cascade.[28–30] We found that BAX expression was increased in *Mpv17*$^{-/-}$ mice, whereas its levels was comparable to WT in *Mpv17*$^{-/-}$*::Opa1*^{tg} littermates (Figures 7B and 7C). In addition, although several cleaved forms of BECLIN-1 were present in WT kidney homogenates, the three previously described, caspase-3 dependent, BECLIN-1 fragments were clearly predominant in *Mpv17*$^{-/-}$ kidney homogenates. In contrast, the same pattern as in the WT was detected in the *Mpv17*$^{-/-}$*::Opa1*^{tg} samples (Figure 7D).

DISCUSSION

Alterations in mitochondrial ultrastructure have an impact on mtDNA stability, as demonstrated, for instance, by the presence of multiple deletions in patients carrying mutations in *OPA1*,[31] *MFN2*,[32] and *ATAD3*.[33] We showed that moderate overexpression of *Opa1* was able to rescue the mtDNA depletion in the "new" genetic background *Mpv17*$^{-/-}$ kidneys, resulting in a markedly prolonged median lifespan from 75 to 553 days. However, the maximum lifespan was similar in *Mpv17*$^{-/-}$ and *Mpv17*$^{-/-}$*::Opa1*^{tg} mice, suggesting that *Opa1* overexpression slowed down but did not completely stop the disease progression, as confirmed by the histological data. One hypothesis that could explain the reason why about 25% of the "new" *Mpv17*$^{-/-}$ model survived as much as the *Mpv17*$^{-/-}$*::Opa1*^{tg} littermates is that not all of them would have inherited the genetic modifier(s) or combination of polymorphisms leading to the more severe phenotype.

Although the MPV17 function remains unclear, mutations in its encoding gene constitute a prominent cause of mtDNA instability

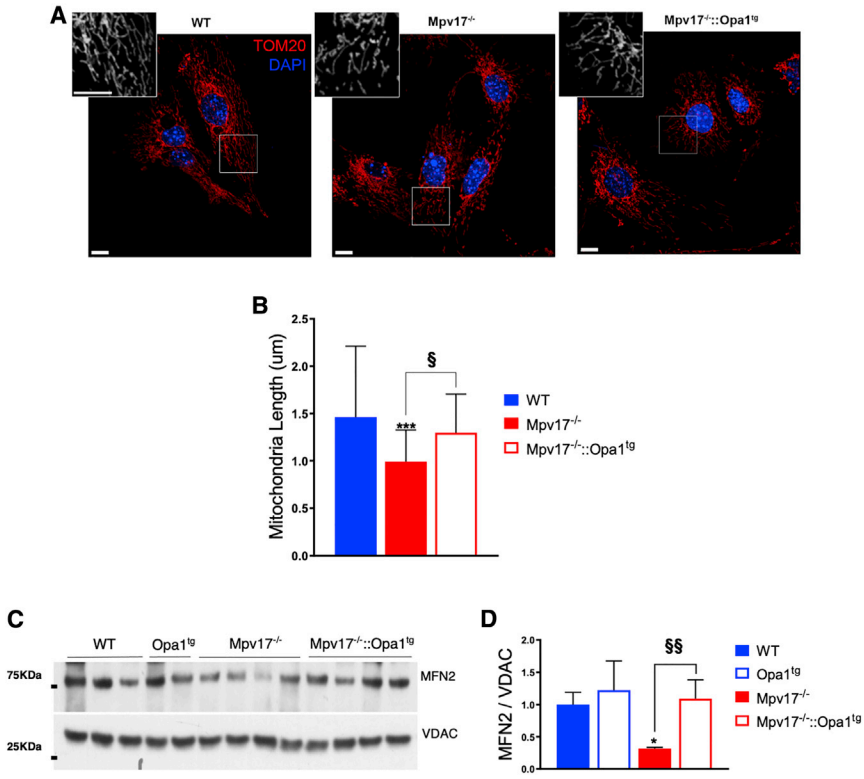

Figure 4. Analysis of Isolated Podocytes

(A) Confocal micrographs indicating mitochondrial morphology (TOM20 in red) and nuclei (DAPI in blue) of podocytes from described genotypes. Maximum intensity projection of z stacks is indicated. Scale bars: 10 μm. (B) Mitochondrial length analysis from (A). Data are plotted as means ± SD (n = 3). Total mitochondria (particles) per condition: 5,663 for WT, 5,107 for *Mpv17*$^{-/-}$, and 4,360 for *Mpv17*$^{-/-}$*::Opa1*$^{+/+}$. Symbols * and § represent the significance levels of *Mpv17*$^{-/-}$*::Opa1*^{tg} versus WT and *Mpv17*$^{-/-}$, respectively, calculated by unpaired t test. ***p = 0.0003 (*Mpv17*$^{-/-}$ vs. WT); §p = 0.0001 (*Mpv17*$^{-/-}$*::Opa1*^{tg} vs. *Mpv17*$^{-/-}$). (C) Western blot immunovisualization with an anti-MFN2 antibody in kidney homogenates. An anti-VDAC antibody was used as a loading control. (D) Densitometric analysis of the western blot in (C). Symbols * and § represent the significance levels of *Mpv17*$^{-/-}$*::Opa1*^{tg} versus WT and *Mpv17*$^{-/-}$, respectively, calculated by two-way ANOVA with Tukey's post hoc multiple comparison test. *p = 0.0218 (*Mpv17*$^{-/-}$ vs. WT); §§p = 0.0045 (*Mpv17*$^{-/-}$*::Opa1*^{tg} vs. *Mpv17*$^{-/-}$).

syndromes in humans. We previously found that mitochondrial cristae ultrastructure was disrupted in the liver of *Mpv17*$^{-/-}$ mice and that mtDNA was decreased to less than 10% of the CTR littermates. However, this was not associated with an overt liver dysfunction unless challenged with a ketogenic high-fat diet, which led to cirrhosis and mouse liver failure.[22] We also reported that *Mpv17*$^{-/-}$ mice developed a late-onset focal segmental glomerulosclerosis, leading to death at around 1.5–2.0 years of age. The early-onset glomerulosclerosis observed after crossing with *Opa1*^{tg} mice was unexpected and remarkably similar to the phenotype originally described,[20] characterized by focal segmental glomerulosclerosis, accumulation of protein casts in the tubuli, and early death. Also the strain we originally reported (a pure C57/6N) developed the same phenotype, but much later, after 12–18 months of life.[19] One question remains unanswered; that is, why 90% mtDNA depletion in liver has little consequence on liver function, whereas partial mtDNA depletion in kidney leads to a very severe, fatal phenotype. One possible explanation is that the kidney is particularly susceptible to oxidative stress.[34] Although we did not measure ROS production in our *Mpv17*$^{-/-}$ mice, this was previously reported in the same mouse model.[35] However, the sudden shift in the phenotype prompted us to hypothesize the presence of causative variants in one of the supposed genetic modifiers of the *Mpv17*$^{-/-}$ mitochondrial phenotypes. The first candidate gene was *Prkdc*, encoding the catalytic subunit of the DNA-PK, which forms a heterotrimer with the Ku p70/YRCC6-p86/XRCC5 proteins in DNA double-strand break repair and recombination. A spontaneous mutation R2140C in *Prkdc* was found in some mouse strains, leading to profound decrease in the amount of the protein, which was proposed to modify the severity of *Mpv17* kidney disease.[24] However, our mice did not carry the *Prdkc* hypomorphic mutant allele.

A second potential modifier of the *Mpv17*$^{-/-}$ phenotype was the nicotinamide nucleotide transhydrogenase (*Nnt*), which regulates NAD(P)H levels by coupling hydride transfer between NAD(H) and NADP(+) to proton translocation across the IMM,[36] thus regulating redox poise. C57BL/6J mice carry two spontaneous mutations in the *Nnt* gene: a missense (methionine-to-threonine) mutation in the mitochondrial leader sequence and an in-frame deletion that removes exons 7–11, resulting in the expression of a truncated, non-functional protein. The mutant *Nnt* allele was previously proposed to impact on the severity of mtDNA mutations.[25] However, although we detected both the WT and truncated forms of the *Nnt* gene in the individuals of our colony, these variants did not segregate with the disease. These results conclusively suggest that other modifiers, or combinations of polymorphisms, may be responsible for the shift in the phenotype. RNA-seq analysis showed a few quantitative differences between the "old" KO and the "new" KO strains, including only two mitochondrial targeted gene products, an unknown transporter (*Slc25a48*) and uridine phosphorylase 2 (*Upp2*). These observations, as well as the few hundred SNP variants identified in the same RNA-seq experiment, warrant validation and further investigation.

Mitochondrial cristae are controlled by a molecular network formed by the MICOS complex, the F_1F_o-ATP synthase, the IMM pleiotropic

Please cite this article in press as: Luna-Sanchez et al., *Opa1* Overexpression Protects from Early-Onset *Mpv17*$^{-/-}$-Related Mouse Kidney Disease, Molecular Therapy (2020), https://doi.org/10.1016/j.ymthe.2020.06.010

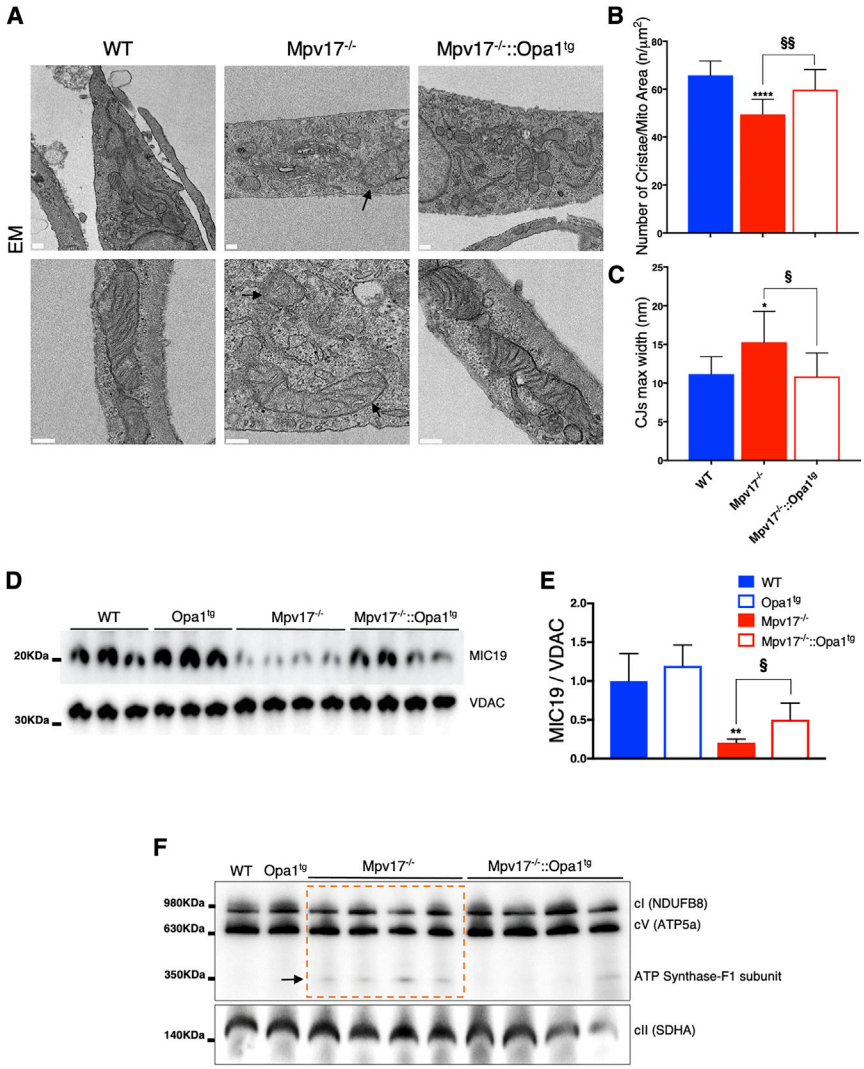

Figure 5. Analysis of Mitochondrial Cristae Morphology

(A) Representative TEM images of isolated podocytes for the indicated genotypes. Scale bars: 200 nm. (B) Quantification of the number of cristae per mitochondrial area from TEM pictures (n = 3 per genotype). Data plotted are mean ± SD (n = 3) of CJ maximum width. Symbols * and § represent the significance levels of *Mpv17*$^{-/-}$*::Opa1*^{tg} versus WT and *Mpv17*$^{-/-}$, respectively, calculated by one-way ANOVA with Tukey's post hoc multiple comparison test. ****p < 0.0001 (*Mpv17*$^{-/-}$ vs. WT); §§p = 0.0068 (*Mpv17*$^{-/-}$*::Opa1*^{tg} versus *Mpv17*$^{-/-}$). (C) Quantification of CJ maximum width from TEM pictures (n = 3). Symbols * and § represent the significance levels of *Mpv17*$^{-/-}$*::Opa1*^{tg} versus WT and *Mpv17*$^{-/-}$, respectively, calculated by one-way ANOVA with Tukey's post hoc multiple comparison test. *p = 0.0182 (*Mpv17*$^{-/-}$ vs. WT); §p = 0.0109 (*Mpv17*$^{-/-}$*::Opa1*^{tg} vs. *Mpv17*$^{-/-}$). (D) Western blot immunovisualization using an anti MFN2 antibody. VDAC was used as a loading control. (E) Densitometric analysis of the western blot in (D). Data are shown as mean ± SD. Symbols * and § represent the significance levels of *Mpv17*$^{-/-}$*::Opa1*^{tg} versus WT and *Mpv17*$^{-/-}$, respectively, calculated by unpaired two-tailed Student's t test. **p = 0.0058 (*Mpv17*$^{-/-}$ vs. WT); §p = 0.0037 (*Mpv17*$^{-/-}$*::Opa1*^{tg} vs. *Mpv17*$^{-/-}$). (F) 1D-BNGE using anti-cI (NDUFB8) and anti-cV (ATP5A) antibodies. cII subunit SDHA was used as a loading control. Note the accumulation of ATP synthase F1 subunits in *Mpv17*$^{-/-}$ mitochondria.

OPA1 protein, and the non-bilayer-forming phospholipids cardiolipin and phosphatidylethanolamine.[27] OPA1 has been shown to be epistatic to MICOS,[37] and its protective effect against mitochondrial dysfunction is mediated by the stabilization of cristae morphology as well as ATP synthase.[38] We found that *Opa1* overexpression was able to correct mitochondrial ultrastructure and increase mtDNA content in the kidney of "new" *Mpv17*$^{-/-}$ mice. mtDNA is bound to the IMM, and altered cristae morphology has an impact on mtDNA maintenance.[31,39–41] Stabilization of the cristae morphology by increased OPA1 expression can, thus, lead to increased mtDNA levels. Interestingly, OPA1 protein levels were reduced in the "new" *Mpv17*$^{-/-}$ mice, possibly as a consequence of cristae alterations. In keeping with this, *Opa1* mRNA levels were normal in *Mpv17*$^{-/-}$ mice. However, while the effect on liver mtDNA was modest, the mtDNA increase in kidney was sufficient to preserve the activities of MRC complexes to WT levels. In addition, our data show that the correction of mitochondrial ultrastructure also stabilized respiratory complexes and SCs. The only exception to this is cIII, whose activity was similar in *Mpv17*$^{-/-}$*::Opa1*^{tg} and *Mpv17*$^{-/-}$ kidneys. One possible explanation is that cIII is more efficiently incorporated in respiratory SCs and/or engaged in respiration, which is, indeed, normal in oxygen consumption studies and in-gel activities (Figure S4), thus contributing to the therapeutic effect. However, the C57BL/6 background makes it particularly difficult to draw conclusions, as SCs have been reported to be almost absent in this background, particularly in kidneys.[42] However, we acknowledge that this is a very controversial issue.[43] Anyway, it should also be noted that *Opa1* overexpression led to ATP synthase stabilization. The 1D-BNGE western blot data, indeed, show the accumulation of free F_1 ATP-synthase particles in *Mpv17*$^{-/-}$, which were absent in *Mpv17*$^{-/-}$*::Opa1*^{tg} kidneys, confirming that *Opa1* overexpression contributes to the stabilization of OXPHOS. These results are in agreement with recent published data.[38] The normalization of mitochondrial ultrastructure explains the reduced apoptosis in *Mpv17*$^{-/-}$*::Opa1*^{tg} versus *Mpv17*$^{-/-}$ kidneys and podocytes. This process may be boosted by the block of BECLIN-1 processing.

Overall, our results further support the deleterious role of cristae disruption in the pathogenic mechanisms leading to organ failure in mitochondrial disorders and the correcting effects of moderate

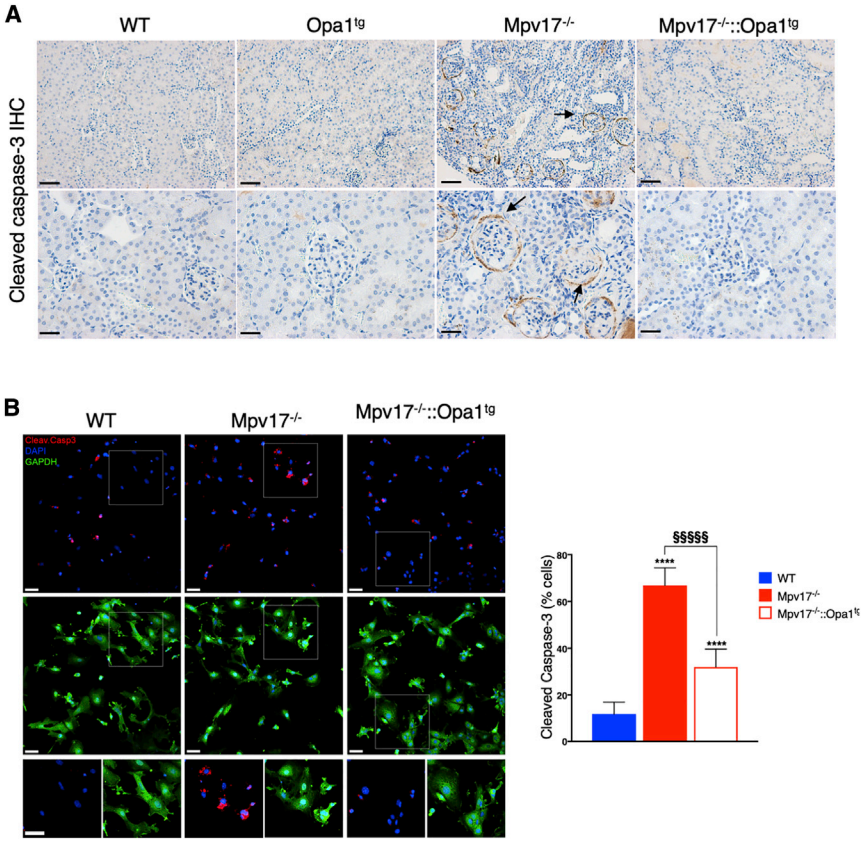

Figure 6. Caspase-3 Staining in Kidney Sections and Isolated Podocytes

(A) Immunohistochemical staining with anti-caspase-3 antibody. Scale bars: 50 μm (upper row) and 20 μm (lower row). (B) Confocal micrographs from primary podocytes derived from described genotypes showing cytoplasm staining (GAPDH in green), apoptotic cells (cleaved caspase-3 in red) and nuclei (DAPI in blue). Maximum intensity projection of z stacks is indicated. Scale bars: 50 μm. On the right panel, quantification of caspase-3-positive cells. Data are presented as mean ± SD. Symbols * and § represent the significance levels versus WT and *Mpv17*$^{-/-}$, respectively, calculated by one-way ANOVA with Tukey's post hoc multiple comparison test. ****p < 0.0001 (*Mpv17*$^{-/-}$ vs. WT, and *Mpv17*$^{-/-}$*::Opa1*^{tg} vs. WT); §§§§p < 0.0001 (*Mpv17*$^{-/-}$*::Opa1*^{tg} versus *Mpv17*$^{-/-}$).

overexpression of *Opa1*, which can be exploited for future therapeutic approaches.

MATERIALS AND METHODS

RNA-Seq Analysis

RNA was extracted by using a standard TRIzol-based protocol from kidney tissue. RNA-seq was carried out by the Next Generation Sequencing (NGS) facility, Department of Pathology, University of Cambridge, Cambridge, UK. A detailed description of the methodology followed for the collection and analysis of data is reported in the Supplemental Materials and Methods.

Antibodies

Antibodies used were: mouse monoclonal anti-GAPDH (1:1,000; ab8245; Abcam), rabbit monoclonal anti-TOM20 Alexa Fluor 647 (1:500; ab209606; Abcam), Alexa Fluor 488 Goat anti-mouse (1:300; A11004; Invitrogen), Alexa Fluor 647 Goat anti-rabbit (1:300; A27040; Invitrogen), rabbit polyclonal anti-NPHS2 (1:300; ab50339; Abcam), mouse monoclonal anti-CYTOKERATIN (1:300; #ab86734; Abcam), and anti-cleaved caspase-3 (1:200; Cell Signaling, #9661).

Chemicals

All chemicals were from Merck-Sigma Aldrich.

Animals

All animal experiments were carried out in accordance with the UK Animals (Scientific Procedures) Act 1986 (PPL: P6C20975A) and EU Directive 2010/63/EU. *Mpv17*$^{+/-}$ and *Opa1*^{tg} original strains were on C57BL/6N and C57BL/6J backgrounds, respectively. *Mpv17*$^{+/-}$*::Opa1*$^{+/tg}$ mice were mated to generate *Mpv17*$^{-/-}$*::Opa1*^{tg} animals. *Mpv17*$^{+/-}$*::Opa1*$^{+/+}$ and *Mpv17*$^{+/+}$*::Opa1*$^{+/+}$ were used as controls, as no differences were observed between *Mpv17*$^{+/+}$ and *Mpv17*$^{+/-}$ mice. Since the *Opa1* transgene is located on the X chromosome, only homozygous females and hemizygous males were considered in this study. The animals were maintained in a temperature- and humidity-controlled animal-care facility with a 12-h:12-h light:dark cycle and free access to water and food and were sacrificed by cervical dislocation.

Isolation of Primary Podocytes

Kidneys were removed from 7- to 10-day-old mice, washed in Ca^2- and Mg^2-free Hank's medium (Thermo Fisher Scientific), and treated with 1.5 mg/mL collagenase type I (Sigma-Aldrich) for 1 min at 37°C. The reaction was stopped by growth medium consisting of Dulbecco's modified Eagle's medium/F-12 (Thermo Fisher Scientific) supplemented with 10% fetal bovine serum (FBS; GIBCO), 1× insulin-transferrin-selenium-ethanolamine (Thermo Fisher Scientific), 1 μM hydrocortisone (Sigma Aldrich), 1× penicillin-streptomycin, and 2 mM L-glutamine (Sigma-Aldrich).

Glomeruli were isolated by sieving through the 100-μm mesh (Fisherbrand) and seeded in 100-mm dishes precoated overnight at 4°C with collagen type IV (Sigma-Aldrich). Cells were kept at 37°C in a 5% CO_2 atmosphere for 7 days. Additional sieving was performed through the 40-μm mesh resuspending the cells with trypsin-EDTA. Cells were plated on dishes or coverslips treated with poly-L-lysine (Sigma-Aldrich) and, the next day, fixed for the respective

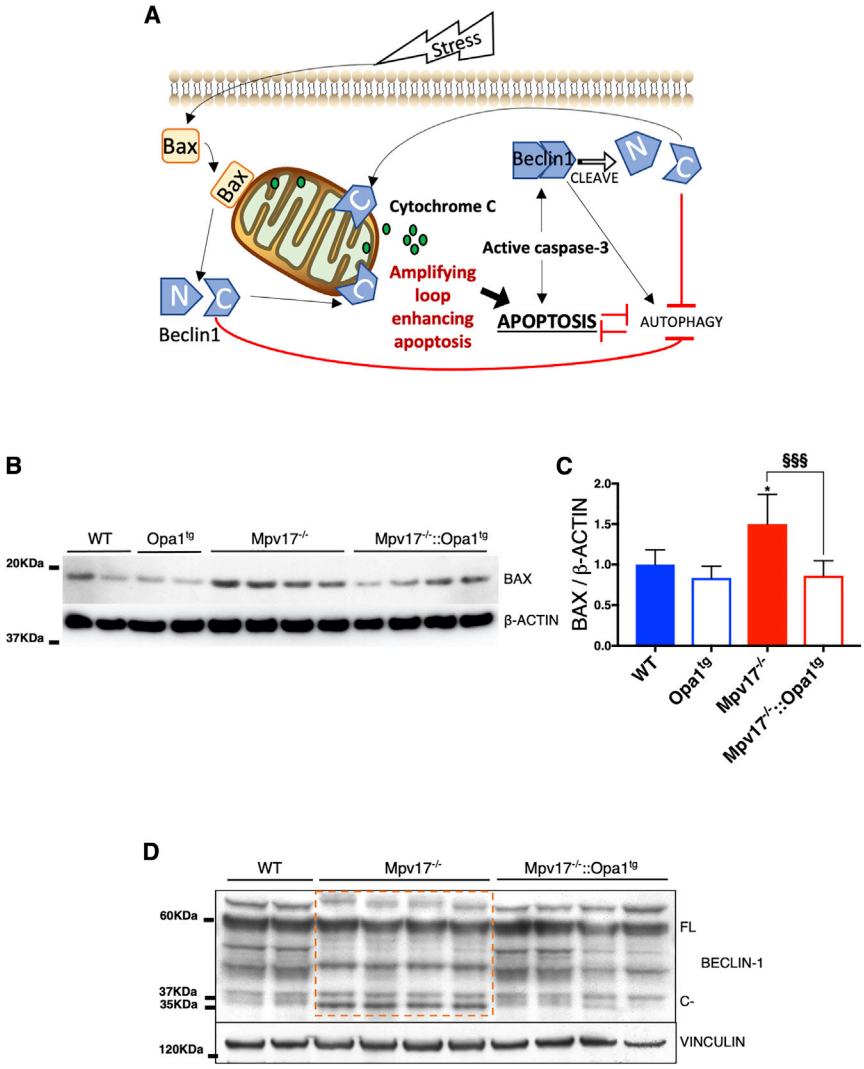

Figure 7. Interplay between Apoptosis and Autophagy through Regulation of BECLIN-1

(A) Schematic representation of the pathway connecting apoptosis and autophagy via modulation of BECLIN-1 processing. Details are given in the text. (B) Western blot immunovisualization of kidney homogenates using an anti-BAX antibody. (C) Densitometric analysis of the western blot in (B). Data are presented as mean ± SD (n = 4 WT; n = 8 KOS). Symbols * and § represent the significance levels of *Mpv17*$^{-/-}$*::Opa1*^{tg} versus WT and *Mpv17*$^{-/-}$, respectively, calculated by one-way ANOVA with Tukey's post hoc multiple comparison test. *p = 0.0176 (*Mpv17*$^{-/-}$ versus WT); §§§p = 0.0008 (*Mpv17*$^{-/-}$*::Opa1*^{tg} *versus Mpv17*$^{-/-}$). (D) Western blot analysis of kidney homogenates using an anti-BECLIN-1 antibody. Note the different pattern of BECLIN-1 processing in *Mpv17*$^{-/-}$ compared to WT and *Mpv17*$^{-/-}$*::Opa1*^{tg} kidneys.

technique. Cell characterization was performed by immunofluorescence using the podocyte (NPHS2) and epithelial cell (cytokeratin) markers.

Immunofluorescence and Imaging

Cells were fixed with 3.7% formaldehyde in F-12 complete media and permeabilized with 0.1% in PBS with 0.1% Triton X-100 and 0.05% sodium deoxycholate before staining with primary and secondary antibodies in blocking solution (5% goat serum). Coverslips were mounted with ProLong Glass with or without DAPI (Invitrogen).

Images were acquired randomly for each slide using a Dragonfly Spinning Disk imaging system (Andor Technologies), composed with a Nikon Ti-E microscope, a Nikon 100× TIRF ApoPlan or 20× ApoPlan objective, and an Andor iXon EMCCD or Zyla sCMOS camera. The z stacks were acquired using Fusion software (Andor Technologies), and the 3D images were analyzed and exported using Imaris software (Bitplane). For mitochondria length measurements of 3, preparation of podocytes (n = 3) per group was used, and several regions of interest (ROIs) were drawn in the peripheric regions of the mitochondrial network using ImageJ.[44] Automatic threshold was used, and "particles" (mitochondria) bigger than 0.05 μm^2 were analyzed. Cleaved caspase-3 analysis was performed by manually counting the number of DAPI- and GAPDH-positive cells and caspase-3-positive cells (n = 3).

TEM

For TEM analysis, mice were subjected to perfusion with the fixative solution (2.5% glutaraldehyde [Sigma-Aldrich], 2% paraformaldehyde [MP Biomedicals] in 0.1 M PB buffer [Sigma-Aldrich]), 1-mm^3 pieces of kidney were kept in fixative solution overnight, and samples were washed several times in 0.1 M phosphate buffer for the following days. For fibroblasts, 1 × 10^6 fibroblasts were fixed in the fixative solution for 1 h at room temperature (RT) in agitation. Cells were scraped, centrifuged (2,500 rpm for 10 min at 4°C), and washed 3 times with 0.1 M PB buffer. Pelleted cells were sent to the Electron Microscopy Platform (Scientific and Technological Centers, University of Barcelona, Barcelona, Spain) for sample preparation. Regions containing the glomeruli were selected, and ultrathin (55-nm) sections were cut, for kidney and cells, and mounted on 200-mesh copper grids with carbon-supported film. Image acquisition (Digital Micrograph, v1.85.1535, Gatan, Pleasanton, CA, USA) was performed with a transmission electron microscope (FEI Tecnai G2 Spirit Twin) coupled with an charge-coupled device (CCD) camera (Orius-SC200B, Gatan, Pleasanton, CA, USA). Quantification of number and width of cristae was performed manually

using ImageJ; 10 cells were analyzed for each genotype (n = 3), number of cristae was counted per visible mitochondria area, and maximum CJ width was determined by randomly measuring 3–4 CJs per mitochondria. Foot process was measured by the ratio between maximum height and width touching the glomerular basement membrane. The mean of this ratio (foot process aspect ratio) was calculated from 21 randomly chosen segments per group (n = 3).

Immunoblotting

Mouse tissues were homogenized in 10 vol of 10 mM potassium phosphate buffer (pH 7.4). Mitochondrial-enriched fractions were collected after centrifugation at 800 × g for 10 min in the presence of protease inhibitors and were frozen and thawed three times in liquid nitrogen. Protein concentration was determined by the Lowry method. Aliquots, 30 μg each, were run through a 12% SDS-PAGE and electroblotted onto a polyvinylidene fluoride (PVDF) membrane, which was then immunodecorated with different antibodies.

For BNGE analysis, brain mitochondria, isolated as previously described,[45] were resuspended in 1.5 M aminocaproic acid, 50 mM Bis-Tris-HCl (pH 7), and 4 mg DDM per milligram of proteins and incubated for 5 min on ice before centrifuging at 20,000 g at 4°C. 5% Coomassie G250 was added to the supernatant. 100 μg was separated by 4%–12% gradient BNGE and electroblotted on nitrocellulose membranes for immunodetection.

Spectrophotometric Analysis of Respiratory Chain Activities

Tissues were snap-frozen in liquid nitrogen and homogenized in 10 mM phosphate buffer (pH 7.4). The spectrophotometric activity of cI and CS was measured as previously described.[46]

Morphological Analysis

For histological and immunohistochemical analyses, animals were fixed in 10% neutral buffered formalin (NBF) for a few days at RT and then included in paraffin wax. 4-μm-thick sections were used for analysis. H&E staining was performed by standard methods. Immunohistochemistry was performed using the Novolink Polymer Detection System and specific antibodies against the indicated proteins.

Statistical Analysis

All numerical data are expressed as mean ± SD. One- or two-way ANOVAs with Tukey correction were used for multiple comparisons (see figure legends for details); Kaplan-Meier distribution and log-rank test were used for survival probability analysis. Differences were considered statistically significant when $p < 0.05$.

SUPPLEMENTAL INFORMATION

Supplemental Information can be found online at https://doi.org/10.1016/j.ymthe.2020.06.010.

AUTHOR CONTRIBUTIONS

C.V., L.S., M.L.-S., and M.Z. designed the study. M.L.-S. performed the *in vivo* experiments, the biochemical assays, the oxygraphy experiments, and the molecular analysis. R.C. performed the histological and histochemical analyses. C.B. and M.L.-S. performed the experiments on primary podocytes. C.B. and A.Y. performed the TEM experiments. G.B.-C. performed the CoQ pool analysis. M.L.-S., C.B., and R.C. analyzed the data. C.V., M.L.-S., C.B., and M.Z. wrote the manuscript.

CONFLICTS OF INTEREST

The authors declare no competing interests.

ACKNOWLEDGMENTS

Our research was supported by the Telethon Foundation, Italy (grant GGP19007), ERC Advanced grant FP7-3222424, and a grant from the NRJ-Institut de France (to M.Z.); Associazione Luigi Comini ONLUS; and a core grant from the Medical Research Council, UK (grant MC_UU_00015/5). We are grateful to the MRC-Laboratory of Molecular Biology Electron Microscopy Facility for access to their resources. We thank Ana B. Cortés at UPO for support in CoQ measurements and Dr. Erika Fernandez-Vizarra, Dr. Aurora Gomez-Duran, and Pedro Pinheiro for their help and advice. We are grateful to Dr. Silvia Armelloni, the Renal Research Laboratory, Fondazione IRCCS Cà Granda Ospedale Maggiore Policlinico, Milan, Italy for sharing the protocol to isolate podocytes.

REFERENCES

1. Viscomi, C., and Zeviani, M. (2020). Strategies for fighting mitochondrial diseases. J. Intern. Med. *287*, 665–684.
2. Civiletto, G., Varanita, T., Cerutti, R., Gorletta, T., Barbaro, S., Marchet, S., Lamperti, C., Viscomi, C., Scorrano, L., and Zeviani, M. (2015). Opa1 overexpression ameliorates the phenotype of two mitochondrial disease mouse models. Cell Metab. *21*, 845–854.
3. Varanita, T., Soriano, M.E., Romanello, V., Zaglia, T., Quintana-Cabrera, R., Semenzato, M., Menabò, R., Costa, V., Civiletto, G., Pesce, P., et al. (2015). The OPA1-dependent mitochondrial cristae remodeling pathway controls atrophic, apoptotic, and ischemic tissue damage. Cell Metab. *21*, 834–844.
4. Spinazzola, A., Viscomi, C., Fernandez-Vizarra, E., Carrara, F., D'Adamo, P., Calvo, S., Marsano, R.M., Donnini, C., Weiher, H., Strisciuglio, P., et al. (2006). MPV17 encodes an inner mitochondrial membrane protein and is mutated in infantile hepatic mitochondrial DNA depletion. Nat. Genet. *38*, 570–575.
5. Karadimas, C.L., Vu, T.H., Holve, S.A., Chronopoulou, P., Quinzii, C., Johnsen, S.D., Kurth, J., Eggers, E., Palenzuela, L., Tanji, K., et al. (2006). Navajo neurohepatopathy is caused by a mutation in the MPV17 gene. Am. J. Hum. Genet. *79*, 544–548.
6. Piekutowska-Abramczuk, D., Pronicki, M., Strawa, K., Karkucińska-Więckowska, A., Szymańska-Dębińska, T., Fidziańska, A., Więckowski, M.R., Jurkiewicz, D., Ciara, E., Jankowska, I., et al. (2014). Novel c.191C>G (p.Pro64Arg) MPV17 mutation identified in two pairs of unrelated Polish siblings with mitochondrial hepatoencephalopathy. Clin. Genet. *85*, 573–577.
7. Uusimaa, J., Evans, J., Smith, C., Butterworth, A., Craig, K., Ashley, N., Liao, C., Carver, J., Diot, A., Macleod, L., et al. (2014). Clinical, biochemical, cellular and molecular characterization of mitochondrial DNA depletion syndrome due to novel mutations in the MPV17 gene. Eur. J. Hum. Genet. *22*, 184–191.
8. Baumann, M., Schreiber, H., Schlotter-Weigel, B., Löscher, W.N., Stucka, R., Karall, D., Strom, T.M., Bauer, P., Krabichler, B., Fauth, C., et al. (2019). MPV17 mutations

in juvenile- and adult-onset axonal sensorimotor polyneuropathy. Clin. Genet. *95*, 182–186.

9. Choi, Y.-R., Hong, Y.B., Jung, S.-C., Lee, J.H., Kim, Y.J., Park, H.J., Lee, J., Koo, H., Lee, J.S., Jwa, D.H., et al. (2015). A novel homozygous MPV17 mutation in two families with axonal sensorimotor polyneuropathy. BMC Neurol. *15*, 179.

10. Blakely, E.L., Butterworth, A., Hadden, R.D.M., Bodi, I., He, L., McFarland, R., and Taylor, R.W. (2012). MPV17 mutation causes neuropathy and leukoencephalopathy with multiple mtDNA deletions in muscle. Neuromuscul. Disord. *22*, 587–591.

11. Garone, C., Rubio, J.C., Calvo, S.E., Naini, A., Tanji, K., Dimauro, S., Mootha, V.K., and Hirano, M. (2012). MPV17 Mutations Causing Adult-Onset Multisystemic Disorder With Multiple Mitochondrial DNA Deletions. Arch. Neurol. *69*, 1648–1651.

12. Antonenkov, V.D., Isomursu, A., Mennerich, D., Vapola, M.H., Weiher, H., Kietzmann, T., and Hiltunen, J.K. (2015). The Human Mitochondrial DNA Depletion Syndrome Gene MPV17 Encodes a Non-selective Channel That Modulates Membrane Potential. J. Biol. Chem. *290*, 13840–13861.

13. Reinhold, R., Krüger, V., Meinecke, M., Schulz, C., Schmidt, B., Grunau, S.D., Guiard, B., Wiedemann, N., van der Laan, M., Wagner, R., et al. (2012). The channel-forming Sym1 protein is transported by the TIM23 complex in a presequence-independent manner. Mol. Cell. Biol. *32*, 5009–5021.

14. Dalla Rosa, I., Cámara, Y., Durigon, R., Moss, C.F., Vidoni, S., Akman, G., Hunt, L., Johnson, M.A., Grocott, S., Wang, L., et al. (2016). MPV17 Loss Causes Deoxynucleotide Insufficiency and Slow DNA Replication in Mitochondria. PLoS Genet. *12*, e1005779.

15. Moss, C.F., Dalla Rosa, I., Hunt, L.E., Yasukawa, T., Young, R., Jones, A.W.E., Reddy, K., Desai, R., Virtue, S., Elgar, G., et al. (2017). Aberrant ribonucleotide incorporation and multiple deletions in mitochondrial DNA of the murine MPV17 disease model. Nucleic Acids Res. *45*, 12808–12815.

16. Alonzo, J.R., Venkataraman, C., Field, M.S., and Stover, P.J. (2018). The mitochondrial inner membrane protein MPV17 prevents uracil accumulation in mitochondrial DNA. J. Biol. Chem. *293*, 20285–20294.

17. Martorano, L., Peron, M., Laquatra, C., Lidron, E., Facchinello, N., Meneghetti, G., Tiso, N., Rasola, A., Ghezzi, D., and Argenton, F. (2019). The zebrafish orthologue of the human hepatocerebral disease gene *MPV17* plays pleiotropic roles in mitochondria. Dis. Model. Mech. *12*, dmm037226.

18. Dallabona, C., Marsano, R.M., Arzuffi, P., Ghezzi, D., Mancini, P., Zeviani, M., Ferrero, I., and Donnini, C. (2010). Sym1, the yeast ortholog of the MPV17 human disease protein, is a stress-induced bioenergetic and morphogenetic mitochondrial modulator. Hum. Mol. Genet. *19*, 1098–1107.

19. Viscomi, C., Spinazzola, A., Maggioni, M., Fernandez-Vizarra, E., Massa, V., Pagano, C., Vettor, R., Mora, M., and Zeviani, M. (2009). Early-onset liver mtDNA depletion and late-onset proteinuric nephropathy in Mpv17 knockout mice. Hum. Mol. Genet. *18*, 12–26.

20. Weiher, H., Noda, T., Gray, D.A., Sharpe, A.H., and Jaenisch, R. (1990). Transgenic mouse model of kidney disease: insertional inactivation of ubiquitously expressed gene leads to nephrotic syndrome. Cell *62*, 425–434.

21. O'Bryan, T., Weiher, H., Rennke, H.G., Kren, S., and Hostetter, T.H. (2000). Course of renal injury in the Mpv17-deficient transgenic mouse. J. Am. Soc. Nephrol. *11*, 1067–1074.

22. Bottani, E., Giordano, C., Civiletto, G., Di Meo, I., Auricchio, A., Ciusani, E., Marchet, S., Lamperti, C., d'Amati, G., Viscomi, C., and Zeviani, M. (2014). AAV-mediated liver-specific MPV17 expression restores mtDNA levels and prevents diet-induced liver failure. Mol. Ther. *22*, 10–17.

23. Cogliati, S., Frezza, C., Soriano, M.E., Varanita, T., Quintana-Cabrera, R., Corrado, M., Cipolat, S., Costa, V., Casarin, A., Gomes, L.C., et al. (2013). Mitochondrial cristae shape determines respiratory chain supercomplexes assembly and respiratory efficiency. Cell *155*, 160–171.

24. Papeta, N., Zheng, Z., Schon, E.A., Brosel, S., Altintas, M.M., Nasr, S.H., Reiser, J., D'Agati, V.D., and Gharavi, A.G. (2010). Prkdc participates in mitochondrial genome maintenance and prevents Adriamycin-induced nephropathy in mice. J. Clin. Invest. *120*, 4055–4064.

25. McManus, M.J., Picard, M., Chen, H.-W., De Haas, H.J., Potluri, P., Leipzig, J., Towheed, A., Angelin, A., Sengupta, P., Morrow, R.M., et al. (2019). Mitochondrial DNA Variation Dictates Expressivity and Progression of Nuclear DNA Mutations Causing Cardiomyopathy. Cell Metab. *29*, 78–90.e5.

26. Kühl, I., Miranda, M., Atanassov, I., Kuznetsova, I., Hinze, Y., Mourier, A., Filipovska, A., and Larsson, N.G. (2017). Transcriptomic and proteomic landscape of mitochondrial dysfunction reveals secondary coenzyme Q deficiency in mammals. eLife *6*, e30952.

27. Colina-Tenorio, L., Horten, P., Pfanner, N., and Rampelt, H. (2020). Shaping the mitochondrial inner membrane in health and disease. J. Intern. Med. *287*, 645–664.

28. Hill, S.M., Wrobel, L., and Rubinsztein, D.C. (2019). Post-translational modifications of Beclin 1 provide multiple strategies for autophagy regulation. Cell Death Differ. *26*, 617–629.

29. Luo, S., and Rubinsztein, D.C. (2013). BCL2L11/BIM: a novel molecular link between autophagy and apoptosis. Autophagy *9*, 104–105.

30. Wirawan, E., Vande Walle, L., Kersse, K., Cornelis, S., Claerhout, S., Vanoverberghe, I., Roelandt, R., De Rycke, R., Verspurten, J., Declercq, W., et al. (2010). Caspase-mediated cleavage of Beclin-1 inactivates Beclin-1-induced autophagy and enhances apoptosis by promoting the release of proapoptotic factors from mitochondria. Cell Death Dis. *1*, e18.

31. Hudson, G., Amati-Bonneau, P., Blakely, E.L., Stewart, J.D., He, L., Schaefer, A.M., Griffiths, P.G., Ahlqvist, K., Suomalainen, A., Reynier, P., et al. (2008). Mutation of OPA1 causes dominant optic atrophy with external ophthalmoplegia, ataxia, deafness and multiple mitochondrial DNA deletions: a novel disorder of mtDNA maintenance. Brain *131*, 329–337.

32. Vielhaber, S., Debska-Vielhaber, G., Peeva, V., Schoeler, S., Kudin, A.P., Minin, I., Schreiber, S., Dengler, R., Kollewe, K., Zuschratter, W., et al. (2013). Mitofusin 2 mutations affect mitochondrial function by mitochondrial DNA depletion. Acta Neuropathol. *125*, 245–256.

33. Peralta, S., Goffart, S., Williams, S.L., Diaz, F., Garcia, S., Nissanka, N., Area-Gomez, E., Pohjoismäki, J., and Moraes, C.T. (2018). ATAD3 controls mitochondrial cristae structure in mouse muscle, influencing mtDNA replication and cholesterol levels. J. Cell Sci. *131*, jcs217075.

34. Coppolino, G., Leonardi, G., Andreucci, M., and Bolignano, D. (2018). Oxidative Stress and Kidney Function: A Brief Update. Curr. Pharm. Des. *24*, 4794–4799.

35. Zwacka, R.M., Reuter, A., Pfaff, E., Moll, J., Gorgas, K., Karasawa, M., and Weiher, H. (1994). The glomerulosclerosis gene Mpv17 encodes a peroxisomal protein producing reactive oxygen species. EMBO J. *13*, 5129–5134.

36. Kampjut, D., and Sazanov, L.A. (2019). Structure and mechanism of mitochondrial proton-translocating transhydrogenase. Nature *573*, 291–295.

37. Glytsou, C., Calvo, E., Cogliati, S., Mehrotra, A., Anastasia, I., Rigoni, G., Raimondi, A., Shintani, N., Loureiro, M., Vazquez, J., et al. (2016). Optic Atrophy 1 Is Epistatic to the Core MICOS Component MIC60 in Mitochondrial Cristae Shape Control. Cell Rep. *17*, 3024–3034.

38. Quintana-Cabrera, R., Quirin, C., Glytsou, C., Corrado, M., Urbani, A., Pellattiero, A., Calvo, E., Vázquez, J., Enríquez, J.A., Gerle, C., et al. (2018). The cristae modulator Optic atrophy 1 requires mitochondrial ATP synthase oligomers to safeguard mitochondrial function. Nat. Commun. *9*, 3399.

39. Gerhold, J.M., Cansiz-Arda, Ş., Lõhmus, M., Engberg, O., Reyes, A., van Rennes, H., Sanz, A., Holt, I.J., Cooper, H.M., and Spelbrink, J.N. (2015). Human Mitochondrial DNA-Protein Complexes Attach to a Cholesterol-Rich Membrane Structure. Sci. Rep. *5*, 15292.

40. Rajala, N., Gerhold, J.M., Martinsson, P., Klymov, A., and Spelbrink, J.N. (2014). Replication factors transiently associate with mtDNA at the mitochondrial inner membrane to facilitate replication. Nucleic Acids Res. *42*, 952–967.

41. Elachouri, G., Vidoni, S., Zanna, C., Pattyn, A., Boukhaddaoui, H., Gaget, K., Yu-Wai-Man, P., Gasparre, G., Sarzi, E., Delettre, C., et al. (2011). OPA1 links human mitochondrial genome maintenance to mtDNA replication and distribution. Genome Res. *21*, 12–20.

42. Cogliati, S., Calvo, E., Loureiro, M., Guaras, A.M., Nieto-Arellano, R., Garcia-Poyatos, C., Ezkurdia, I., Mercader, N., Vázquez, J., and Enriquez, J.A. (2016). Mechanism of super-assembly of respiratory complexes III and IV. Nature *539*, 579–582.

43. Milenkovic, D., Blaza, J.N., Larsson, N.-G., and Hirst, J. (2017). The Enigma of the Respiratory Chain Supercomplex. Cell Metab. *25*, 765–776.

44. Schindelin, J., Arganda-Carreras, I., Frise, E., Kaynig, V., Longair, M., Pietzsch, T., Preibisch, S., Rueden, C., Saalfeld, S., Schmid, B., et al. (2012). Fiji: an open-source platform for biological-image analysis. Nat. Methods *9*, 676–682.

45. Fernández-Vizarra, E., López-Pérez, M.J., and Enriquez, J.A. (2002). Isolation of biogenetically competent mitochondria from mammalian tissues and cultured cells. Methods *26*, 292–297.

46. Bugiani, M., Invernizzi, F., Alberio, S., Briem, E., Lamantea, E., Carrara, F., Moroni, I., Farina, L., Spada, M., Donati, M.A., et al. (2004). Clinical and molecular findings in children with complex I deficiency. Biochim. Biophys. Acta *1659*, 136–147.